Ocean mixing and heat transport processes observed under the Ross Ice Shelf control its basal melting

Craig Stevens[a,b,1], Christina Hulbe[c], Mike Brewer[a], Craig Stewart[a], Natalie Robinson[a], Christian Ohneiser[d], and Stefan Jendersie[e]

[a]Ocean Dynamics Group, New Zealand National Institute of Water and Atmospheric Research, Wellington 6241, New Zealand; [b]Department of Physics, University of Auckland, Auckland 1010, New Zealand; [c]Department of Surveying, University of Otago, Dunedin 9016, New Zealand; [d]Department of Geology, University of Otago, Dunedin 9054, New Zealand; and [e]Antarctic Research Centre, Victoria University of Wellington, Wellington 6140, New Zealand

Edited by Jeffrey P. Severinghaus, Scripps Institution of Oceanography, La Jolla, CA, and approved May 20, 2020 (received for review June 23, 2019)

The stability of large Antarctic ice shelves has important implications for global sea level, sea ice area, and ocean circulation. A significant proportion of ice mass loss from these ice shelves is through ocean-driven melting which is controlled by largely unobserved oceanic thermodynamic and circulatory processes in the cavity beneath the ice shelf. Here we use direct measurements to provide evidence of the changing water column structure in the cavity beneath the Ross Ice Shelf, the planet's largest ice shelf by area. The cavity water column data exhibit both basal and benthic boundary layers, along with evidence of tidally modulated and diffusively convecting internal mixing processes. A region of thermohaline interleaving in the upper–middle water column indicates elevated diffusion and the potential to modify the cavity circulation. The measurements were recorded using the Aotearoa New Zealand Ross Ice Shelf Program hot water drill borehole melted in the central region of the shelf in December 2017 (HWD2), only the second borehole through the central region of the ice shelf, following J9 in 1977. These data, and comparison with the 1977 data, provide valuable insight into ice shelf cavity circulation and aid understanding of the evolution of the presently stable Ross Ice Shelf.

ice shelf cavity | ocean mixing | interleaving | basal melting | Antarctic oceanography

The cavities beneath Antarctic ice shelves are among the least sampled components of the climate system. Yet, ice shelf retreat is today the leading driver of change in the grounded Antarctic ice sheet, and ocean forcing is, in turn, an important driver of change in ice shelves (1, 2). Ice shelf basal melting is theorized to occur by 1) circulation of cold, High-Salinity Shelf Water (HSSW) to the grounding line where it is above the in situ melt temperature; 2) intrusion of relatively warm, modified Circumpolar Deep Water (mCDW) into the cavity; and 3) circulation of Antarctic Surface Water (AASW), in particular, its seasonally warmer upper layer, under the ice shelf (3–6). High-resolution models capable of simulating melting driven by these water masses as they flow under an ice shelf (e.g., refs. 7–9) are too resource-intensive for long-term projections which instead rely on simplified parameterizations (e.g., ref. 10). As well as resolving the basal boundary layer, simulations need to address tidal timescales as salt and heat exchanges at the ice shelf base are modulated by tidal currents; this is thought to be particularly important in cold-water systems like the Ross Ice Shelf (RIS) or the Filchner–Ronne (11, 12). With new observations from the center of the RIS cavity, our motivating questions are the following: 1) Is the ice melting? 2) Has the ocean cavity system changed since it was last observed four decades ago? 3) Given the almost total absence of direct, fine-scale observations, does the system work as expected?

The RIS is the largest ice shelf by area on the planet (~4.7×10^5 km^2). While not regarded as under immediate threat from accelerated melting, the RIS is downstream of the West Antarctic Ice Sheet and is known to have changed rapidly in the past (13). Furthermore, connectivity between ice shelves is potentially a driver of ice shelf and sheet evolution, and the RIS is oceanically downstream of the rapidly melting Amundsen Sea ice shelves (14). With a cavity residence timescale of less than 6 y (15–17), it is reasonable to expect that the RIS is experiencing the effects of climate change already.

The present data are from the HWD2 borehole, located initially at 80°39.497 °S, 174° 27.678 °E (Fig. 1 and *Methods*) and 300 km from the ice shelf front. The site is predicted to be on the western flank of an outward flowing zone of the ocean cavity with speeds of between 1 to 2 (18) and 5 cm s^{-1} (19), but it is clear that the circulation varies on small scales relative to the horizontal dimensions of the cavity (19). While the margins of the RIS cavity have been previously sampled (11, 16, 20), the central cavity has been sampled only once previously. This was during the Ross Ice Shelf Project J9 borehole work in the mid-1970s at a site 335 km southeast of HWD2 (*SI Appendix*). The J9 sampling found a 250-m-deep ocean cavity with a three-layered structure in terms of salinity and temperature (21, 22) and a refreezing basal boundary (23). Models and observations suggest two distinct regimes. Deep within the cavity, melt rates are low, with broad regions of slow (O ~ 1 cm/y) freezing predicted by models

Significance

This study describes measurements of the ocean beneath the center of the Ross Ice Shelf, the Earth's largest ice shelf. Ice shelves experience melting from below by the ocean and so are vulnerable to a warming climate system. We present the second dataset ever collected from this region, the first having been gathered 40 y prior. Our data provide a basis for better understanding the complex processes that drive melting. They illustrate the degree of variability in the mid-water column, a region largely ignored in modeling. We also observed ephemeral refreezing on the ice shelf underside, with implications for both melt rate and upper ocean dynamics. This insight emphasizes the importance of in situ observations in undersampled environments.

Author contributions: C. Stevens, C.H., and N.R. designed research; C. Stevens, M.B., and C.O. performed research; C. Stevens and S.J. contributed new reagents/analytic tools; C. Stevens, C. Stewart, N.R., and C.O. analyzed data; and C. Stevens, C.H., and C. Stewart wrote the paper.

The authors declare no competing interest.

This article is a PNAS Direct Submission.

Data deposition: Data have been deposited at https://www.seanoe.org/data/00629/74128/.

[1]To whom correspondence may be addressed. Email: craig.stevens@niwa.co.nz.

This article contains supporting information online at https://www.pnas.org/lookup/suppl/doi:10.1073/pnas.1910760117/-/DCSupplemental.

First published June 29, 2020.

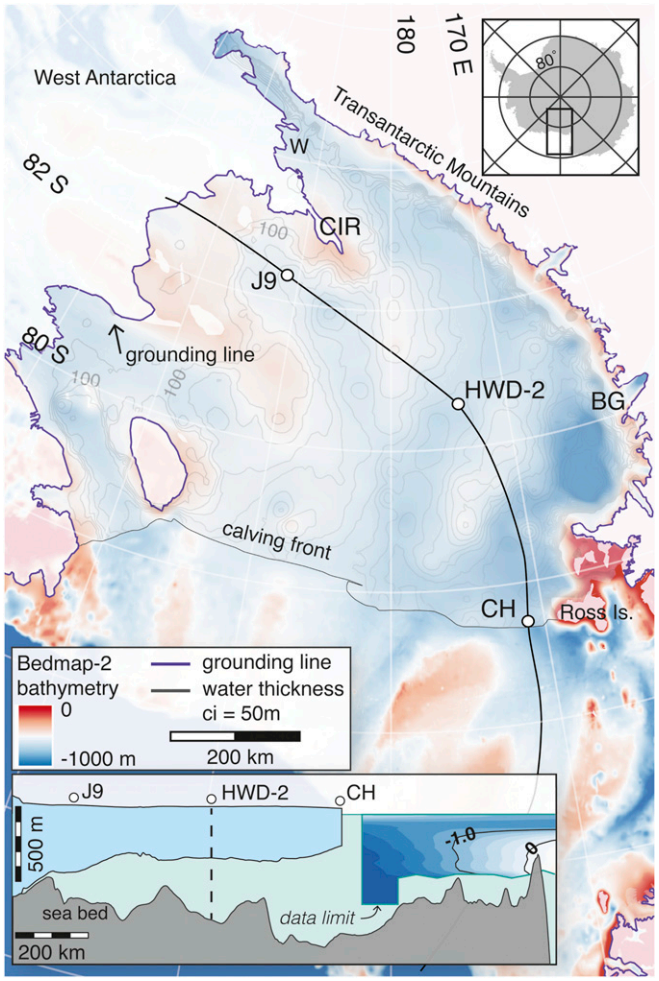

Fig. 1. Location and bathymetry. Location of the HWD-2 borehole in the RIS. Depth of the seabed is shown in the range from 0 to −1,000 m from the Bedmap-2 dataset (28). The purple line shows the grounding line where the grounded ice sheet first goes afloat. Gray lines are contours of constant water column thickness. Areas covered by grounded ice sheet are shaded white. The Moderate Resolution Imaging Spectroradiometer (MODIS) Image Mosaic of Antarctica is overlain on the ice shelf area as a transparent layer. Ice rises are shaded darker gray. (*Inset*) The floating ice surface and base, and depth of the seafloor along the black line connecting the three RIS borehole locations. Byrd Glacier (BG) and Crary Ice Rise (CIR) are marked along with experiments at J9, WISSARD (W), and Coulman High (CH). The labeled contours show mean annual potential temperature from the World Ocean Atlas (29) with a contour interval of 0.2 °C. The direction of the line is not glaciologically significant, and we note that the relatively thin region between J9 and HWD-2 is in the wake of an ice rise.

(figure 7 in ref. 4 and figure 10 in ref. 15) and inferred from observations (J9). Closer to the ice front, models predict higher mean melt rates (O ~ 1 m/y) and stronger seasonal variability (7, 11, 15, 18, 19, 24), features confirmed by recent observations (5, 25, 26). The largest rates, near the front, are associated with inflow of local summer surface water (5, 27).

Water Column Structure

The HWD2 borehole was opened on 5 December 2017, and water column measurements resolved the mean and variability in the thermohaline conditions. The vertical structure can be divided into four distinct regions, as identified in Fig. 2. A homogenized benthic boundary layer occupies the deepest 20 to 40 m of the water column (region A). Above this lies a linearly stratified zone around 150 m thick (region B). Region C above this, also with thickness ~150 m, exhibited highly variable temperature and salinity structure. This zone was topped by a basal boundary layer just beneath the ice of around 30 m in thickness (region D) where potential temperatures were at, or just above, the local freezing temperature. In S_p–θ_0 space (Fig. 2*D*), the HWD2 thermohaline structure lies between conditions at the grounding line (20) and the ice shelf front (11) but closer to the ice shelf front conditions. Our results connect the ref. 3 boundary conditions and the ocean simulations of ref. 4, with the deep cavity circulation being driven by HSSW, the densest open ocean water mass available at the ice shelf front, which then enters the cavity and follows the bathymetry until it eventually reappears in the central or basal layers.

The time-integrated current observations are unique for the central cavity and show a residual flow of 2 cm s^{-1} toward the

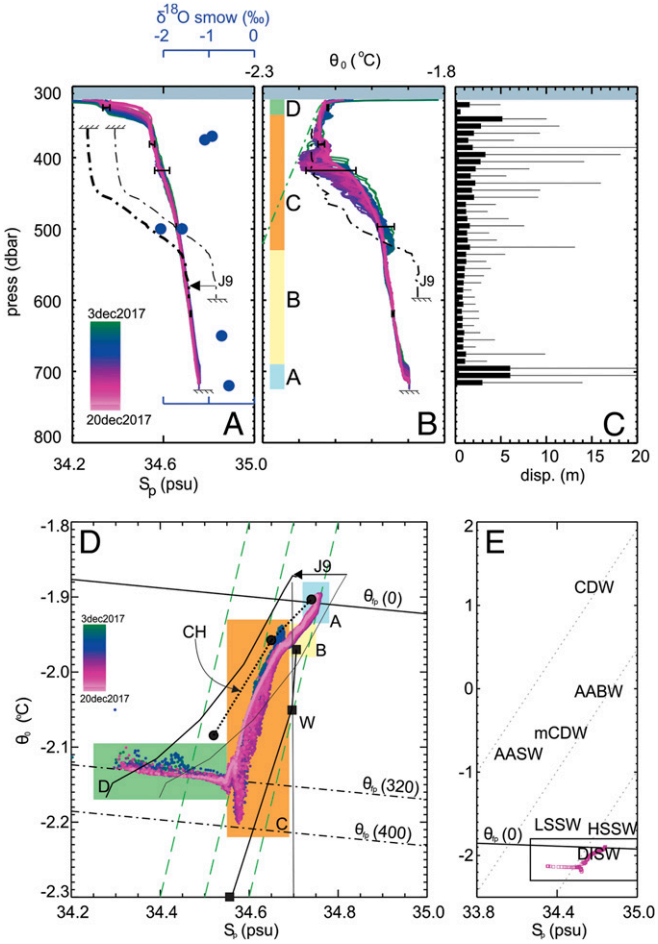

Fig. 2. Thermohaline structure. (*A*) Practical salinity S_p (and oxygen isotopes) and (*B*) potential temperature θ_0 profiles with example profiles from J9 included for comparison (with freshened J9 salinity included) with regions A to D as discussed in *Water Column Structure*. The horizontal bars show variability in the data from the mooring sensors. (*C*) Vertical displacement scale based on density showing average (thick) and maximum (thin) estimates in 10-m bins (*Methods*). (*D*) Practical salinity vs. potential temperature with regions as discussed in *Water Column Structure* as well as example Gade lines. This includes representative S_p–θ_0 structure from Coulman High (CH; ref. 11), J9 (ref. 20, plus freshened equivalent), and WISSARD (W; ref. 18 converted from TEOS-10). (*E*) The broader view of S_p vs. θ_0 shows water masses including AASW, Antarctic Bottom Water (AABW), Circumpolar Deep Water and mCDW, HSSW and LSSW, and DISW, and the region of *E* is marked as a box. The water column vertical extent in the various field campaigns shown in Fig. 2*D* expands from 10 m at WISSARD (20), through 250 m at J9, 400 m at HWD2, and then 600 m at Coulman High (11).

open ocean (Fig. 3). This speed extends through most of the water column but is slower by a factor of 2 in the uppermost measurements. Simulations in ref. 18 show the cavity circulation is dominated by a central core flowing oceanward in the middle of the cavity and that the HWD2 location is on the western flank of this flow. Our observations imply a residence time for water passing this point of around 4 y (*Methods*), which lies within the ranges estimated by modeling [2.2 (17) and 6 y (15)] and inferred from ocean measurement (1 to 6 y; e.g., ref. 16).

Basal Boundary Layer and Melting vs. Freezing

The basal boundary layer is the oceanic layer just beneath the ice where melting and refreezing takes place. Its thickness (region D in Fig. 2), based on profiles of temperature and salinity, varied between 15 and 20 m, at times bounded on the underside by a warmer band dynamically constrained by the reduced salinity layer above. Temperatures in the layer are generally within 20 mK of in situ freezing temperature. The vertical structure in the layer was characterized by smooth variability rather than sharp discontinuities (which would otherwise indicate diffusive-convective mechanics or shear-induced coherent features), so the melting here is not influenced by diffusive convective processes as seen in the George VI ice shelf basal boundary layer (30).

Oblique imagery shows a thin (~10 cm) layer of ice crystals on the ice underside. In something of a contradiction, visual observations within the borehole itself indicated sediment within the ice, right to the basal boundary (Fig. 4*A*) but not in the crystal layer itself. This indicates that there is no substantial marine ice layer, as found in refreezing ice shelf regions (31), and implies that the crystal layer is ephemeral. This is consistent with the borehole location being within a band of ice characterized via airborne radar as lacking a basal marine layer and possibly containing englacial debris near the base (32).

Temperature and salinity observations support the notion of slow and intermittent melting. Despite the presence of crystals on ice shelf underside, observations indicate water temperatures ranging from 0 to 8 mK above the in situ freezing point at the ice base. Using methodologies for estimating melt and freeze rates (33, 34), these levels of thermal driving (35) indicate melt rates of 0 to 0.09 m a^{-1}. Available estimates of the spatial distributions of melt rate (e.g., refs. 4, 36) suggest that the HWD2 site is representative of processes occurring over a substantial proportion of the ice shelf. The upper end of this range of melt rates is close to an estimated mean ice shelf melt rate of 0.076 m a^{-1} (37). However, the presence of the crystals fixed to the ice underside, paradoxically present during weakly melting conditions, implies elevated surface roughness (38, 39), which may increase the rate of melt/freeze by as much as a factor of 2.5.

Taken together, these observations indicate a basal environment close to the melt/freeze threshold. Basal melting is parameterized as a function of instantaneous flow speed, through its influence on boundary layer mixing (40). The instantaneous flow is a combination of mean flow and tides but dominated by these tides (Fig. 3). The profiled observations span more than half of the spring to neap tide conditions where the diurnal tides change amplitude by a factor of around 5 (Fig. 3). Presently available data show the integrated flow to be in a direction toward 15 to 20 TN, approximately parallel to the local lines of constant water column thickness (Fig. 1).

Midcolumn Mixing and Interleaving

The basal melting supply of freshwater results in a top-to-bottom variation in salinity of 0.4 psu, comparable to that observed offshore of the cavity (16). The midcolumn structure is characterized by a gradually time-varying set of perturbations in salinity and temperature water. The salinity and temperature structure interleave (Fig. 3*D* and *SI Appendix*, Fig. S2), and there is clear evidence of turbulent mixing (Fig. 3*D*). It is unlikely that there is sufficient shear to drive mixing, which leaves double diffusion as the primary source of mixing as suggested at the vertically constrained WISSARD (Whillans Ice Stream Subglacial Access Research Drilling) grounding-line water column (20). However, we did not observe classic diffusive convective layering of consistent steps in temperature and salinity (e.g., ref. 41).

In region C, regardless of the driver, there appears to be persisting instability, with overturns occasionally extending over 10 m in the vertical. This structure is not consistent over the sampling period but evolves from profile to profile (*SI Appendix*, Fig. S2), and temperatures drop to the in situ freezing point at times. This water must have interacted with the ice base at 400 m depth or deeper. The closest point with 400 m draft is toward Crary Ice Rise; however, considering the likely cavity circulation, this water mass might also be from the keel of the Byrd Glacier a similar distance away to the west (Fig. 1). The $\delta^{18}O$ data suggest water more depleted in $\delta^{18}O$ compared with oceanic observations across the front of the RIS (42). This suggests a melt water contribution from ice of significant age (43).

The interleaving in this region is not consistently statically stable. Many of the profiles exhibit overturns in the density structure, particularly as the lunar phase enters spring tide conditions near the end of the profile sampling, around day of year 352 (18 December 2017; *SI Appendix*, Fig. S3). In addition, through the first half of the sampling period, a unique water mass is present around the base of region C that appears in Fig. 2*D* as a distinct branch on the S_p–θ_0 curve (−1.95 °C, 34.675 psu). This disappears completely for the second half of the sampling, so either the driver of the variability is switched off (but not for upper part of region C), or the cavity circulation changes so that this water mass is no longer observed at this location. Either way, the

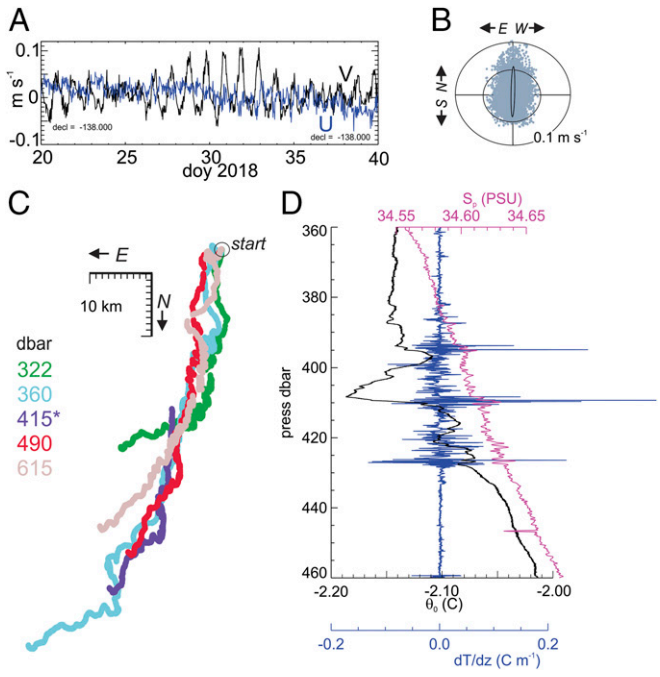

Fig. 3. Kinematics and fine structure. Velocity distribution from current meters showing (*A*) 20-d time series segment for upper current meter (U east–west component in blue) and (*B*) instantaneous velocity scatterplot with the combined K1 and O1 tidal ellipse for the upper sensor. (*C*) Integrated progressive vector for all five sensors over 35 d (asterisk indicates that the sensor at 415 m did not start reliably reporting until several weeks after the other instruments, so its starting point is arbitrary). (*D*) Mid-water column section of temperature, salinity, and temperature gradient from a microstructure profile.

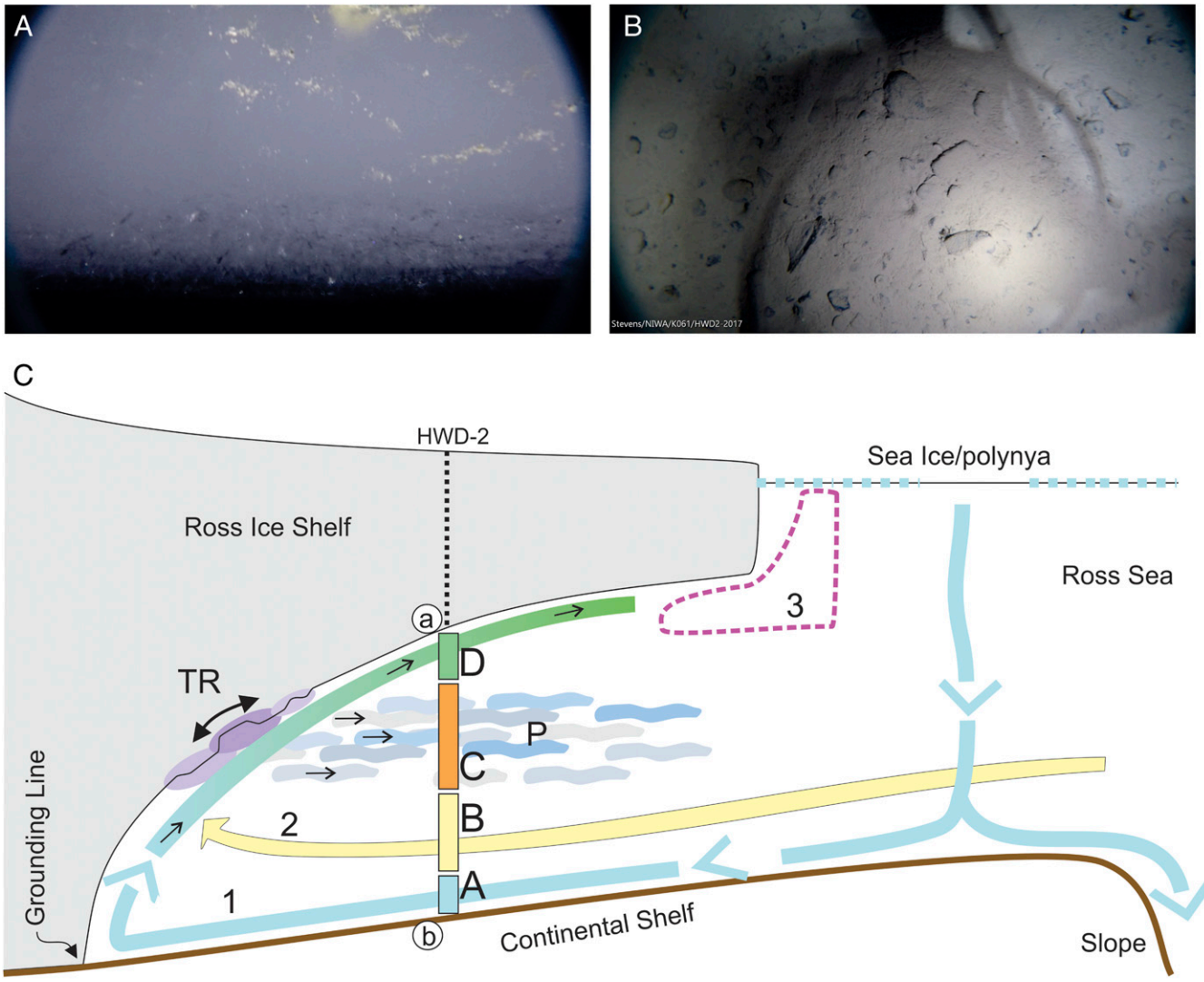

Fig. 4. Visual imagery (expanded in *SI Appendix*, Fig. S4) from video showing (*A*) oblique wide-angle view of ice underside showing crystals and (*B*) downward view of seafloor (image ∼60 cm across). (*C*) Speculative sketch of cavity behavior showing regions identified in Fig. 2. The pathways 1, 2, and 3 refer to modes identified in ref. 3, and TR is tide–roughness interaction. The a and b in circles refer to the images. The open water influence via modes 1 and 2 moves southward [mode 3 likely does not penetrate as far south as HWD2 (5, 27)] and either drives or is entrained into the basal boundary layer. At some point this boundary layer encounters basal variations that result in tidally driven mixing (varying with the spring–neap cycle) which results in patches of water P with varying T and S signatures moving out into the cavity.

implication is that the cavity is heterogeneous in its density and diffusivity structures. An estimate of vertical diffusivity based on these overturns is $K_z \sim 1 \times 10^{-3}$ m^2 s^{-1} (*Methods*), which is orders of magnitude greater than molecular diffusivities. A length scale for vertical diffusion over a period equivalent to half the residence timescale, ∼250 m, is comparable to cavity depth. While the observed overturn sections do not extend over the full depth of the water column (*SI Appendix*, Fig. S2), the analysis indicates that enhanced diffusion implied by the layering is a major contributor to cavity dynamics in that it has the potential to modify the expected circulation.

Benthic Boundary Layer

The basal boundary layer flow at HWD2 varies in thickness from 20 to 40 m over the sampling period (region A in Fig. 2). It flows over a substrate composed of ∼5-cm clasts in a mantle of fine mud (Fig. 4*B*). We were unable to place a velocity sensor sufficiently near the bed, so we have no direct velocity data in this bottom layer. However, flows above this region were tidally dominated and reached 0.1 m s^{-1} (Fig. 3) comparable to the CATS2008 inverse model updated from ref. 44 (and also see *SI Appendix*, Fig. S3). The salinity just above the seabed is the only portion of the water column that can be identified as HSSW. Salinity transitions smoothly across the upper side of this boundary layer (Fig. 2*A* at around 690 to 710 dbar) while the faster-diffusing temperature exhibits a step (Fig. 2*B* at around 690 to 710 dbar); this apparent contradiction suggests there must be resupply of water at the deepest temperature (i.e., $\theta_0 = -1.9$ °C). Considering water temperature as a quasi-passive short-term tracer, the implication is that HSSW inflow in this region is discrete and relatively thin. Ref. 7 suggests that the circulation is controlled by the tectonic imprint. The animations of penetration of warmer water supplementary to ref. 7 show the southward penetration is along quite specific pathways. The present in situ data suggest that we have intersected a narrow layer of unknown extent which must be influenced by small-scale bathymetric variability.

Comparing with the transects along the ice shelf front of (16) and allowing for nearly 2 decades of freshening (45), the region A temperature and salinity properties come from the western side of the cavity front. At shorter timescales, the variation in depth of the top of the HWD2 benthic boundary layer exhibited two minima ∼9 d apart, suggesting possible modulation by the spring–neap cycle (*SI Appendix*, Fig. S3). The deepest depth for the benthic boundary layer upper bound occurred around 2 d after minimum (neap) tidal amplitude. The isotherm depth at the top of the benthic boundary layer varied over ∼5 m in any sampling burst, indicating high frequency variability, likely oscillations at the benthic boundary layer interface.

Water Masses

The temperature and salinity conditions suggest that other than the boundary layer regions, water properties conform to Deep Ice Shelf Water (DISW), possibly sourced from Low-Salinity Shelf Water (LSSW; Fig. 2*E*) or a mixture of HSSW and LSSW and AASW. The Gade lines (*Methods*) in Fig. 2*D* suggest that the HWD2 profile intersects two circulation pathways whereby regions A and C fall on separate lines. The near grounding line WISSARD results lie mostly on the Gade line evolving from the region A starting point, although the middle of the profile does not conform perfectly, and this may be indicative of nonlinear mixing processes inherent in diffusive–convective mixing. Region D, within 20 m of the ice base, has distinctly different thermohaline characteristics to the remainder of the water column, and the effects of ice–ocean interactions are most apparent here. Within this layer, salinity varies by 0.25 psu, more than the entire remaining 400 m of the water column. Despite this, temperatures remain clustered around the in situ freezing point and are potentially created by rising meltwater plumes, formed from LSSW and raised to the in situ freezing point by frazil ice production.

Our findings have significant implications for modeling of ice shelf cavities. A meaningful predictive tool must resolve a well-defined basal boundary layer. The present observations indicate as much as 20 to 30 m of the upper water column—where phase change takes place—is influenced by melting and ice roughness. Beneath this, the central core of the modeled water column must resolve and transport thermohaline fine structure and adequately deal with transient diffusive convective mixing. A consistent observation from HWD2 and J9 is the presence of interleaving, intrusion, and overturns in the mid-water column, features which will increase fluxes of heat and salt. In order to generate the observed behavior, tidal interactions with upper and lower solid boundaries must be adequately represented over a wide spatial domain and so require tide-resolving time steps and sufficient spatial resolution to resolve ice basal topographic features (4, 12, 46). Comparable reliability in benthic topography also appears to be required to adequately resolve what appears to be, at HWD2 at least, a thin inflowing benthic boundary layer that can take advantage of even quite small topographic variations to transport heat toward the grounding line (4, 19, 46, 47).

Model representations of the vertical structure of mixing and stratification that are sufficiently resolved to simulate the essential water column features observed at HWD2 are rare. For example (15), track layer-following distributions of properties in simulations that enable separation of sluggish transport in the interior and pathways for the mixed layer and isopycnic layers beneath. Our conclusion that tidally driven mixing drives intrusions (i.e., the relatively depleted oxygen isotopic signal; Fig. 2*A*), that in turn support diffusive convective conditions in the mid-water column, implies that non–shear-driven molecular processes come to the fore (e.g., ref. 30). The persistence of significant S_p–θ_0 fine-scale structure implies that the models either are overly dissipative or do not generate the driving intrusions. While this situation aids numerical stability, it reduces buoyancy-driven flows and, given the long timescales required for ice sheet projections, is a serious limitation that needs further investigation.

Has the Cavity Water Column Changed Since 1977?

Comparison of water column properties observed in J9 and HWD2 reveals some key differences between the two locations and epochs. Adjusting for the observed Ross Sea 0.03 psu/decade freshening (45), we find that salinity only matches closely (at the same depth) near the bed of J9 and in the lower part of the HWD2 central water column (region B). Above this (region C), salinity is substantially greater at HWD2, so that the apparent midcolumn rate of freshening is reduced within the cavity relative to Ross Sea conditions. This may relate to the recent apparent reversal in salinity trend in the region (48). The distinct S_p–θ_0 signature of the benthic boundary layer (region A) at HWD2 was not observed at J9 or at Coulman High, implying that the identifiable inflow is limited in spatial extent.

Simulations suggest circulation cells divide regions of the cavity (4, 6, 11, 15, 17, 18), and this limits our ability to interpret different conditions at J9 and HWD2 in terms of temporal change in cavity properties. However, one of the more apparent differences between HWD2 and J9 is that the lower cavity interior (region B in Fig. 2) is consistent and stable at HWD2, whereas at J9 the variability was reduced, but comparable with, the upper interior (region C in Fig. 2). This implies that the thinner and more variable water column thickness was driving changes in thermohaline structure in this deeper region (Fig. 4*C*). The J9 water column structure data do not have the basal meltwater seen in HWD2 (region D), or if it is meltwater, it is mixed over a much thicker vertical extent than at HWD2. This implies that supply of heat into the basal boundary layer might be augmented by a flux from beneath, at least on the more weakly ventilated eastern side of the cavity (4).

The HWD2 observations provide compelling evidence that the interior RIS ocean cavity is highly variable in the vertical direction, sufficiently so that vertical diffusivities must be substantially larger than previously considered. In addition, this appears to vary over spring–neap timescales. Advancing our present understanding of cavity circulation and ice shelf basal melting will require improvements in how cavity water column mechanics are represented (Fig. 4*C*). Further, analysis must seek to identify specific drivers of interleaving, must integrate flow observations with cavity circulation simulations, and must examine spatiotemporal variability. Bringing together observed and modeled perspectives is critical for improving our predictions of ice sheet evolution and resulting earth system outcomes.

Methods

The HWD2 Camp was established in October 2017 following from a site survey in 2015. On 5 December 2017 the camp location was 80°39.497′S, 174°27.678′E where the ice is moving seaward at around ∼600 m a^{-1} (49) and is sourced from the Transantarctic Mountains (50). Ground-based seismic surveying has revealed the large-scale subshelf bathymetry (51), altimetry provides estimates of ice shelf draft (52), and cavity volume estimated from numerical representations suggest a volume of around 130 × 10^3 km^3 (4). However, significant uncertainty remains in the cavity geometry (53). This has implications for topographically guided ocean circulation, at both the seafloor and basal boundary.

The HWD2 site is in a modest local minimum in terms of ice thickness (*SI Appendix*, Table S2). Two 25-cm initial diameter boreholes were melted using a hot water drill (based on a design described in ref. 54). The first borehole (HWD2-A) was used for initial camera inspection and a conductivity–temperature–depth (CTD) profile after which an instrumented mooring was deployed. The mooring included Nortek current meters and Seabird SBE 37 CTD instruments. A second borehole (HWD2-B), 500 m to the south along an ice flow trajectory, was kept open for 12 d (9 to 20 December 2017) and used for all subsequent CTD profiles as well as bottle-sampling for oxygen isotope analysis. The majority of the profiling was with an RBR Concerto CTD and was sufficiently well resolved to allow estimation of overturn scales. Some

additional profiles were recorded with a Rockland microstructure profiler (*SI Appendix*).

Data Availability. Data are available from https://www.seanoe.org/data/00629/74128/.

ACKNOWLEDGMENTS. This research was facilitated by the New Zealand Antarctic Research Institute funded Aotearoa New Zealand Ross Ice Shelf Programme and the Victoria University of Wellington Hot Water Drilling initiative. We thank the Victoria University of Wellington Hot Water Drilling Team led by Alex Pyne and Darcy Mendeno. Jeff Dunne, Lana Hastie, and Kurt Roberts made it possible to work at camp. Dan Lowry, Gavin Dunbar, and Gary Wilson provided field assistance and invaluable discussions. Brett Grant, Pete de Joux, and Nick Eaton developed and mobilized the instrumentation. Logistics support and flights were provided by Antarctica New Zealand and Kenn Borek Air. Additional support was provided by New Zealand National Institute of Water and Atmospheric Research Strategic Science Investment Funding, the Deep South National Science Challenge, and the Antarctic Science Platform. We thank two anonymous reviewers for their constructive comments on an earlier draft of this work.

1. Y. Liu *et al*., Ocean-driven thinning enhances iceberg calving and retreat of Antarctic ice shelves. *Proc. Natl. Acad. Sci. U.S.A.* **112**, 3263–3268 (2015).
2. T. A. Scambos *et al*., How much, how fast?: A science review and outlook for research on the instability of Antarctica's Thwaites Glacier in the 21st century. *Global Planet. Change* **153**, 16–34 (2017).
3. S. S. Jacobs, H. H. Helmer, C. S. M. Doake, A. Jenkins, R. M. Frolich, Melting of ice shelves and the mass balance of Antarctica. *J. Glaciol.* **38**, 375–387 (1992).
4. S. Jendersie, M. J. Williams, P. J. Langhorne, R. Robertson, The density-driven winter intensification of the Ross Sea circulation. *J. Geophys. Res.* **123**, 7702–7724 (2018).
5. C. L. Stewart, P. Christoffersen, K. W. Nicholls, M. J. M. Williams, J. A. Dowdeswell, Basal melting of Ross Ice Shelf from solar heat absorption in an ice-front polynya. *Nat. Geosci.* **12**, 435–440 (2019).
6. H. D. Pritchard *et al*., Antarctic ice-sheet loss driven by basal melting of ice shelves. *Nature* **484**, 502–505 (2012).
7. K. J. Tinto *et al*., Ross Ice Shelf response to climate driven by the tectonic imprint on seafloor bathymetry. *Nat. Geosci.* **12**, 441–449 (2019).
8. T. Hattermann, L. H. Smedsrud, O. A. Nøst, J. M. Lilly, B. K. Galton-Fenzi, Eddy-resolving simulations of the Fimbul Ice Shelf cavity circulation: Basal melting and exchange with open ocean. *Ocean Model.* **82**, 28–44 (2014).
9. P. St-Laurent, J. M. Klinck, M. S. Dinniman, Impact of local winter cooling on the melt of Pine Island Glacier, Antarctica. *J. Geophys. Res.* **120**, 6718–6732 (2015).
10. N. R. Golledge *et al*., Global environmental consequences of twenty-first-century ice-sheet melt. *Nature* **566**, 65–72 (2019).
11. I. B. Arzeno *et al*., Ocean variability contributing to basal melt rate near the ice front of Ross Ice Shelf, Antarctica. *J. Geophys. Res.* **119**, 4214–4233 (2014).
12. K. Makinson, P. R. Holland, A. Jenkins, K. W. Nicholls, D. M. Holland, Influence of tides on melting and freezing beneath Filchner-Ronne Ice Shelf, Antarctica. *Geophys. Res. Lett.* **38**, L06601 (2011).
13. G. Catania, C. Hulbe, H. Conway, T. A. Scambos, C. F. Raymond, Variability in the mass flux of the Ross ice streams, West Antarctica, over the last millennium. *J. Glaciol.* **58**, 741–752 (2012).
14. Y. Nakayama, R. Timmermann, C. B. Rodehacke, M. Schröder, H. H. Hellmer, Modeling the spreading of glacial meltwater from the Amundsen and Bellingshausen Seas. *Geophys. Res. Lett.* **41**, 7942–7949 (2014).
15. D. M. Holland, S. S. Jacobs, A. Jenkins, Modelling the ocean circulation beneath the Ross Ice Shelf. *Antarct. Sci.* **15**, 13–23 (2003).
16. W. M. Smethie Jr., Circulation and melting under the Ross Ice Shelf: Estimates from evolving CFC, salinity and temperature fields in the Ross Sea. *Deep Sea Res. Part I Oceanogr. Res. Pap.* **52**, 959–978 (2005).
17. T. E. Reddy, D. M. Holland, K. R. Arrigo, Ross ice shelf cavity circulation, residence time, and melting: Results from a model of oceanic chlorofluorocarbons. *Cont. Shelf Res.* **30**, 733–742 (2010).
18. K. Assmann, H. H. Hellmer, A. Beckmann, Seasonal variation in circulation and water mass distribution on the Ross Sea continental shelf. *Antarct. Sci.* **15**, 3–11 (2003).
19. S. L. Mack, M. S. Dinniman, J. M. Klinck, D. J. McGillicuddy Jr., Modeling ocean eddies on Antarctica's cold water continental shelves and their effects on ice shelf basal melting. *J. Geophys. Res.* **124**, 5067–5084 (2019).
20. C. R. Begeman *et al*., Ocean stratification and low melt rates at the Ross Ice Shelf grounding zone. *J. Geophys. Res.* **123**, 7438–7452 (2018).
21. S. S. Jacobs, A. L. Gordon, J. L. Ardai Jr., Circulation and melting beneath the ross ice shelf. *Science* **203**, 439–443 (1979).
22. T. D. Foster, The temperature and salinity fine structure of the ocean under the Ross Ice Shelf. *J. Geophys. Res.* **88**, 2556–2564 (1983).
23. I. A. Zotikov, V. S. Zagorodnov, J. V. Raikovsky, Core drilling through the ross ice shelf (Antarctica) confirmed Basal freezing. *Science* **207**, 1463–1465 (1980).
24. M. S. Dinniman *et al*., Modeling ice shelf/ocean interaction in Antarctica: A review. *Oceanography (Wash. D.C.)* **29**, 144–153 (2016).
25. H. J. Horgan, R. T. Walker, S. Anandakrishnan, R. B. Alley, Surface elevation changes at the front of the Ross Ice Shelf: Implications for basal melting. *J. Geophys. Res.* **116**, C02005 (2011).
26. A. A. Stern, M. S. Dinniman, V. Zagorodnov, S. W. Tyler, D. M. Holland, Intrusion of warm surface water beneath the McMurdo Ice Shelf, Antarctica. *J. Geophys. Res.* **118**, 7036–7048 (2013).
27. A. Malyarenko, N. J. Robinson, M. J. M. Williams, P. J. Langhorne, A wedge mechanism for summer surface water inflow into the Ross Ice Shelf cavity. *J. Geophys. Res.* **124**, 1196–1214 (2019).
28. L. O. Fretwell *et al*., Bedmap2: Improved ice bed, surface and thickness datasets for Antarctica. *Cryosphere* **7**, 375–393 (2013).
29. T. P. Boyer *et al*., *World Ocean Database 2013, NOAA Atlas NESDIS 72*, S. Levitus, A. Mishonov, Eds. (Silver Spring, MD, technical ed., 2013), 209 pp.
30. S. Kimura, K. W. Nicholls, E. Venables, Estimation of ice shelf melt rate in the presence of a thermohaline staircase. *J. Phys. Oceanogr.* **45**, 133–148 (2015).
31. M. Craven, I. Allison, H. A. Fricker, R. Warner, Properties of a marine ice layer under the Amery Ice Shelf, East Antarctica. *J. Glaciol.* **55**, 717–728 (2009).
32. C. S. Neal, The dynamics of the Ross Ice Shelf revealed by radio echo-sounding. *J. Glaciol.* **24**, 295–307 (1979).
33. A. Jenkins, K. W. Nicholls, H. F. Corr, Observation and parameterization of ablation at the base of Ronne Ice Shelf, Antarctica. *J. Phys. Oceanogr.* **40**, 2298–2312 (2010).
34. A. Jenkins *et al*., West Antarctic Ice Sheet retreat in the Amundsen Sea driven by decadal oceanic variability. *Nat. Geosci.* **11**, 733–738 (2018).
35. D. M. Holland, A. Jenkins, Modeling thermodynamic ice ocean interactions at the base of an ice shelf. *J. Phys. Oceanogr.* **29**, 1787–1800 (1999).
36. G. Moholdt, L. Padman, H. A. Fricker, Basal mass budget of Ross and Filchner-Ronne ice shelves, Antarctica, derived from Lagrangian analysis of ICESat altimetry. *J. Geophys. Res.* **119**, 2361–2380 (2014).
37. M. A. Depoorter *et al*., Calving fluxes and basal melt rates of Antarctic ice shelves. *Nature* **502**, 89–92 (2013).
38. N. J. Robinson, C. L. Stevens, M. G. McPhee, Observations of amplified roughness from crystal accretion in the sub-ice ocean boundary layer. *Geophys. Res. Lett.* **44**, 1814–1822 (2017).
39. M. G. McPhee, C. L. Stevens, I. J. Smith, N. J. Robinson, Turbulent heat transfer as a control of platelet ice growth in supercooled under-ice ocean boundary layers. *Ocean Sci.* **12**, 507–515 (2016).
40. D. R. MacAyeal, Thermohaline circulation below the Ross Ice Shelf: A consequence of tidally induced vertical mixing and basal melting. *J. Geophys. Res.* **89**, 597–606 (1984).
41. M. L. Timmermans, C. Garrett, E. Carmack, The thermohaline structure and evolution of the deep waters in the Canada Basin, Arctic Ocean. *Deep Sea Res. Part I Oceanogr. Res. Pap.* **50**, 1305–1321 (2003).
42. A. Loose, P. Schlosser, W. M. Smethie, S. Jacobs, An optimized estimate of glacial melt from the Ross Ice Shelf using noble gases, stable isotopes, and CFC transient tracers. *J. Geophys. Res. Oceans* **114**, C08007 (2009).
43. T. Sowers, M. Bender, Climate records covering the last deglaciation. *Science* **269**, 210–214 (1995).
44. L. Padman, H. A. Fricker, R. Coleman, S. Howard, S. Erofeeva, A new tidal model for the Antarctic ice shelves and seas. *Ann. Glaciol.* **34**, 247–254 (2002).
45. S. S. Jacobs, C. F. Giulivi, Large multidecadal salinity trends near the Pacific–Antarctic continental margin. *J. Clim.* **23**, 4508–4524 (2010).
46. M. Årthun, P. R. Holland, K. W. Nicholls, D. L. Feltham, Eddy-driven exchange between the open ocean and a sub–ice shelf cavity. *J. Phys. Oceanogr.* **43**, 2372–2387 (2013).
47. M. P. Schodlok, D. Menemenlis, E. Rignot, M. Studinger, Sensitivity of the ice-shelf/ocean system to the sub-ice-shelf cavity shape measured by NASA IceBridge in Pine Island Glacier, West Antarctica. *Ann. Glaciol.* **53**, 156–162 (2012).
48. P. Castagno *et al*., Rebound of shelf water salinity in the Ross Sea. *Nat. Commun.* **10**, 5441 (2019).
49. E. Rignot, J. Mouginot, B. Scheuchl, Ice flow of the Antarctic ice sheet. *Science* **333**, 1427–1430 (2011).
50. C. M. LeDoux, C. L. Hulbe, M. P. Forbes, T. A. Scambos, K. Alley, Structural provinces of the Ross Ice Shelf, Antarctica. *Ann. Glaciol.* **58**, 88–98 (2017).
51. C. R. Bentley, K. C. Jezek, RISS, RISP and RIGGS: Post-IGY glaciological investigations of the Ross Ice Shelf in the US programme. *J. R. Soc. N. Z.* **11**, 355–372 (1981).
52. J. A. Griggs, J. L. Bamber, Antarctic ice-shelf thickness from satellite radar altimetry. *J. Glaciol.* **57**, 485–498 (2011).
53. R. Timmermann *et al*., A consistent data set of Antarctic ice sheet topography, cavity geometry, and global bathymetry. *Earth Syst. Sci. Data* **2**, 261–273 (2010).
54. K. Makinson, P. G. Anker, The BAS ice-shelf hot-water drill: Design, methods and tools. *Ann. Glaciol.* **55**, 44–52 (2014).